On the Reflection, Transmission, Coupling and Damping of Non-Plane Acoustic Modes by Resonator Rings

A. Cárdenas Miranda and W. Polifke
Lehrstuhl für Thermodynamik, Technische Universität München
85747 Garching, Germany
cardenas@td.mw.tum.de

Abstract

A semi-analytical model of a resonator ring composed of cylindrical ducts with reactive and dissipative shell is extended to account for scattering and mode coupling of three dimensional acoustic waves at duct junctions. A "mode-matching" method based on the weak conservation of mass and momentum in an integral sense across the interface by application of the Galerkin approach is used. The method is validated against FEM data of a test case available in the literature. A representative resonator ring used in rocket chambers is also studied. Scattering into higher radial evanescent modes is clearly observed close to the eigenfrequency of the cavities.

1. Introduction

Due to a possible feedback between heat release and acoustics, rocket engines are prone to thermo-acoustic instabilities. Because energy density and efficiency of modern engines are extremely high, the resulting high frequency oscillations can lead to severe anomalies of motor performance and even to the destruction of the thrust chamber in a very short time. Acoustic cavities, so called resonators, are commonly attached to the chamber in order to increase the acoustic losses and thus the stability of the engines. Figure 1 shows a generic thrust chamber with acoustic cavities of the quarter wave type arranged into a resonator ring. It is generally assumed that dissipation of acoustic energy close to the cavity mouths by turbulent losses and along the cavity walls by viscous forces are responsible for the stabilizing influence of resonators. Furthermore, the acoustic field of the chamber interacts with the backing volume of the cavities. In the framework of this project, a three dimensional model that describes the propagation of acoustic waves through resonator rings has been already proposed [1, 2].

The resonator ring is modeled as a cylindrical duct with finite shell impedance, which describes the effects of the cavities. The stabilizing influence of resonators due to dissipative losses has already been corroborated in a generic thrust chamber modeled as a network of low order acoustic elements using the afore mentioned resonator ring element [2]. However, the scattering of acoustic waves at the interface between two duct sections of different shell impedance has been neglected until now. When reaching a discontinuity in the shell boundary, e.g. a jump in shell impedance, acoustic waves will be partially transmitted and partially reflected, especially at frequencies where the cavities are strongly reactive. To account for these effects, the previously mentioned model of the resonator ring is extended to allow such scattering.

In the literature, especially for the optimization of liners used in aeroengines for suppression of noise, several mode matching approaches and discussion on the validity of them can be found [3]. A classical approach used by several authors is to match acoustic pressure and axial velocity at the discontinuity plane in a weak sense [4]. As will be shown in this paper, this is a valid approximation only for cases with vanishing mean flow. For configurations where surface waves, e.g. modes with oscillations only close to pressure release surfaces ($z \approx i\psi$) [5], more accurate approaches exist, which are capable of handling the discontinuity at the leading trailing edge. It is not trivial to determine the direction of propagation of these surface modes, because they may appear as an hydrodynamic instability. In this case, a method based on the Wiener-Hopf technique is proposed by Rienstra [6]. However, as pointed out by Rienstra, in the majority of engineering problems the acoustic impedance at the shell is high enough and surface waves do not usually appear. In those cases, mode matching techniques are well suited.

The paper is organized as follows: first, the resonator ring model will be reviewed before showing the derivation of the so called "mode-matching" technique at the interface between duct sections of different shell impedance. A test case of a circular duct with a segment of finite shell impedance is defined and characterized. For non-reflecting

boundary conditions a solution procedure based on the scattering matrix is given, that describes the propagation of three dimensional transverse waves along the system. A first test case configuration that represents a turbofan inlet is used to validate the method against FEM data available in literature. A second test case configuration that reproduces a representative resonator ring element as used in rocket thrust chambers is finally studied. Consequences of scattering on the stabilizing influence of resonator rings are then discussed.

2. Acoustic field in cylindrical geometries with arbitrarily shell boundary condition

In the presence of a uniform mean flow $\vec{v}_0 = [U_0, 0, 0]^T$ in axial direction, assuming constant speed of sound c_0 and neglecting viscous dissipation, the propagation of acoustic waves in cylindrical ducts with arbitrarily hard or reactive and dissipative shell can be studied by solving the linearized, three-dimensional, convective wave equation for the fluctuating pressure p':

$$\frac{1}{c_0^2}\left(\frac{\partial}{\partial t} + U_0\frac{\partial}{\partial x}\right)^2 p' = \vec{\nabla}^2 p' \quad . \tag{1}$$

Assuming harmonic time dependency and separation of variables, the general solution in cylindrical coordinates can be written as:

$$\frac{p'}{c_0\rho_0} = \sum_{m,n}\left[J_m(\alpha^+_{mn}r)F_{mn}e^{-ik^+_{mn}x} + J_m(\alpha^-_{mn}r)G_{mn}e^{-ik^-_{mn}x}\right]e^{i\omega t}e^{im\theta} = \sum_{m,n}(f_{mn} + g_{mn}) \ , \tag{2}$$

which can be interpreted as three dimensional waves or "modes" of tangential and radial order m and n traveling in the upstream "f" and downstream "g" direction, respectively. The characteristic amplitudes F_{mn} and G_{mn} give information about the relative local sound pressure level. The radial wave numbers $\alpha^{\pm}_{mn}$ determine the transverse mode shape, while the axial wave numbers $k^{\pm}_{mn}$ describe their axial propagation. Both wave numbers are linked to each other by the dispersion relation:

$$k^{\pm}_{mn} = \frac{-M\omega/c \pm \sqrt{(\omega/c)^2 - (\alpha^{\pm}_{mn}/R_c)^2(1-M^2)}}{1-M^2} \ , \tag{3}$$

where R_c is the duct radius and $M = U_0/c_0$ the Mach number. The radial wave numbers depend on the boundary condition on the cylinder shell. In the presence of mean flow and knowing the impedance of the cylinder shell $Z(\omega)$, they can be determined from Myers' boundary condition [7]:

$$-\frac{i\omega}{\rho_0}\frac{\partial p'}{\partial r} = \left(\frac{\partial}{\partial t} + U_0\frac{\partial}{\partial x}\right)^2 \frac{p'}{Z(\omega)} \ , \tag{4}$$

by substituting the general solution of the pressure Eq. (2). For details about the method used to solve this complex valued transcendental equation, refer to [2]. In the hard-wall case the radial velocity fluctuation vanishes $v' = 0|_{r=R_c}$ and thus $Z(\omega) \to \infty$, the radial wave numbers are purely real valued and frequency independent. Furthermore, the upstream and downstream traveling wave have equal mode shape even in the presence of mean flow:

$$\alpha^+_{mn} = \alpha^-_{mn} = \lambda_{mn} = const. \qquad \in \mathbb{R} \ , \tag{5}$$

where λ_{mn} correspond to the roots of the Bessel function derivative. At frequencies beyond the "cut-on" value:

$$f^c_{mn} = \frac{c_0}{2\pi}\frac{\lambda_{mn}}{R_c}\sqrt{1-M^2} \ , \tag{6}$$

the imaginary part of the axial wave numbers vanishes and the transverse mode starts to propagate. For lower frequencies the mode is evanescent and the modal amplitude decays exponentially along the axial direction.

In the soft-wall case with a reactive and dissipative shell of finite impedance $Z(\omega)$, the radial wave numbers are complex valued, frequency dependent and generally different for the positive and negative direction of propagation:

$$\alpha^+_{mn} \neq \alpha^-_{mn} = f(\omega) \qquad \in \mathbb{C} \ . \tag{7}$$

From the linearized momentum equation, the velocity fluctuations can be determined. Introducing the abbreviations

$$\kappa^{\pm}_{mn} = \frac{k^{\pm}_{mn}}{\omega/c_0 - Mk^{\pm}_{mn}} \qquad \text{and} \qquad \beta^{\pm}_{mn} = \frac{1}{\omega/c_0 - Mk^{\pm}_{mn}} \ , \tag{8}$$

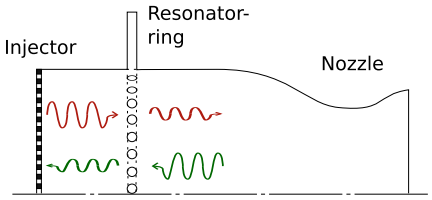

Figure 1: Resonator ring in generic rocket thrust chamber.

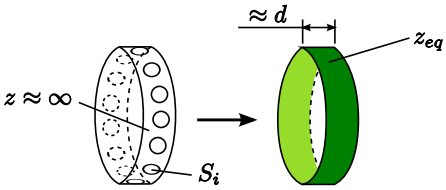

Figure 2: Equivalent specific impedance of a resonator ring homogenized over a portion of the cylinder shell.

they can be written in terms of the characteristic amplitudes f and g:

$$u' = \kappa^+_{mn} f + \kappa^-_{mn} g \ , \tag{9}$$

$$v' = i(\beta^+_{mn} \frac{\partial f}{\partial r} + \beta^-_{mn} \frac{\partial g}{\partial r}) \ , \tag{10}$$

$$w' = -\frac{m}{r}(\beta^+_{mn} f + \beta^-_{mn} g) \ . \tag{11}$$

2.1 Resonator ring model as a soft-wall cylinder

Following a well known technique for linings in aeroengines [8, 4], a resonator ring in rocket thrust chambers can be modeled as a cylindrical duct segment with dissipative and reactive shell boundary of equivalence impedance $Z_{eq}(\omega)$ as shown in Fig. 2. The method has been already introduced and successfully tested [2] for the application of stability prediction in rocket thrust chambers. The dissipation of acoustic energy in the region enclosed by the resonator ring leading to improved stability has been corroborated. However, all effects occurring at the transverse planes where the resonator ring is connected to the rest of the chamber like reflections and mode coupling were not taken into account. In this paper, only the key features of the afore mentioned derivation will be reviewed and the focus will lie on its extension to account scattering and mode coupling at the discontinuity planes.

The starting point is the characterization of a single resonator in terms of its acoustic impedance at the cavity mouth. An expression proposed by Laudien et al. [9] is used in this study:

$$Z(\omega) = \frac{p'}{u'} = \Theta + i\Psi = \left(1 + \epsilon_{nl} + \frac{l_r}{d}\right) \sqrt{8\mu_0\rho_0\omega} - ic_0\rho_0 \cot\left(\frac{\omega l_e}{\bar{c}}\right) \ , \tag{12}$$

where the real part or "resistance" Θ accounts for the dissipation, while the imaginary part or "reactance" Ψ describes the phase shift or time delay. Dissipative effects due to linear viscous forces and turbulent non-linear losses are taken by the resistance into account. At high pressure levels, the non-linear losses dominate and these are modeled, due to the lack of an accurate global model, by an experimentally determined coefficient ϵ_{nl} [10]. The resistance length matches the geometry of the experiment with that of quarter tubes. For the reactance analytical expressions exist for simple geometries. The effective length of the cavities $l_e = l_c + \delta l$ accounts for the the portion of gas taking part in the oscillations. According to Munjal [11], it can be estimated as $\delta l \approx 0.85d$, where d is the cavity diameter. For simplicity the classical case with homogeneous properties inside the cavity and average speed of sound $\bar{c}$ is given here. The eigenfrequencies of the cavities are thus given by the expression

$$f_R = (2n-1)\frac{\bar{c}}{4l_e} \quad , \quad n = 1, 2, 3 \ldots \tag{13}$$

For an array of n_R resonators placed in parallel into a ring, the equivalent homogeneous specific impedance is readily obtained as [9]:

$$z_{eq} = \frac{Z_{eq}}{c\rho A_{ref}} = \left(\sum_j \frac{c\rho A_j}{Z_j}\right)^1 \qquad \rightarrow \qquad z_{eq} = \frac{4Z_R}{n_R \pi d^2 \rho c} \ , \tag{14}$$

where the individual local impedances Z_j are weighted by the free field impedance ρc and the local reaction area A_j and the equivalent impedance by the total area $A_{ref} = 2\pi R_c d = \sum A_j$. Because the portion of the shell with hard boundaries has an infinite impedance (wall-normal velocity is here zero), their effect is inherently taken into account by the weighting area A_{ref}. This procedure corresponds to averaging the impedance over the cylinder shell area as shown in Fig. 2.

Using this equivalent impedance as boundary condition in the previous analysis, the propagation of three dimensional waves through resonator rings can be described. In [2], as a first approximation, the scattering of acoustic waves at the connecting planes between hard- and soft-wall segments has been neglected. As it will be shown in Sec. 4.3 for strong reacting cavities, it actually has to be taken into account. The extension of the model to account for these effects is the aim of the next section.

3. Modal scattering at a shell impedance transition

The expressions presented in Sec. 2 describe the propagation of acoustic waves in segments with homogeneous shell impedance. Due to linearity, the solution may be represented as a summation over modes, which are independent from each other. At a discontinuity caused, for example, by connecting two duct segments of different shell impedance, a relation between the characteristic amplitudes F_{mn} and G_{mn} on both sides of the connecting plane is needed. For the application of resonator rings in rocket thrust chambers we are mainly interested in the scattering at a plane connecting a hard- to a soft-wall duct segment and vice versa. However, the method presented here can be applied to a connecting plane of arbitrary impedance, e.g. two resonator rings equipped with different cavities.

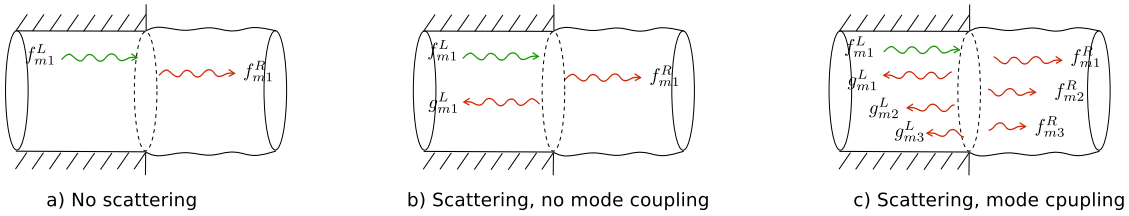

a) No scattering b) Scattering, no mode coupling c) Scattering, mode cpupling

Figure 3: Sketch of three different approaches for the description of a jump in wall impedance.

Consider a cylindrical duct of radius R_c with a discontinuity in the wall impedance at axial position $x = 0$ shown in Fig. 4. The left part of the duct, $x < 0$, has a hard wall at which the radial acoustic velocity vanishes $v'(r = R_c) = 0$. The shell of the right part of the duct, $x > 0$, is characterized by a frequency dependent impedance $z_R = f(\omega)$ and thus, the radial velocity does not necessarily have to be zero. Mode shapes and axial propagation are determined in each segment by the method described in Sec. 2. To close the problem, the characteristic amplitudes $F^{R/L}_{mn}$ and $G^{R/L}_{mn}$ of

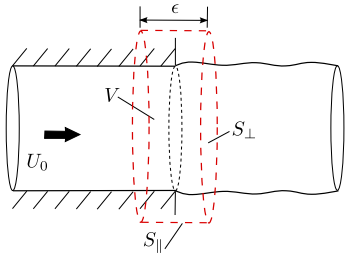

Figure 4: Control volume enclosing a discontinuity in shell impedance.

the corresponding waves on the left and on the right of the discontinuity at position $x = 0$ are needed. This procedure is usually called “mode-matching“. Figure 3 shows three approaches of increasing complexity. In the simplest one, a), all scattering is neglected and an incoming wave is just transmitted. For cases in which the radial wave numbers differ only slightly between the two connected regions, this is a reasonable first approximation. Approach b) allows some scattering, i.e. transmission and reflection, but only in the mode order of the incoming wave. In the more general case, approach c), scattering into different mode orders may occur, too. In this study, we will handle with the last mentioned general case following the linearized mode-matching technique already proposed by Gabard and Astley [12] that preserves mass and momentum across the discontinuity. However, we will start the derivation from the conservation equations in integral form.

3.1 Integral mode-matching

We use here the approach proposed by Gabard and Astle [12]. The basic idea is to derive an expression that preserves mass and momentum in an integral sense across the connecting plane. A control volume enclosing the discontinuity is defined, see Fig. 4. The conservation equations for mass and momentum in integral form are the starting point for the derivation:

$$\iiint_V \frac{\partial \rho}{\partial t} dV + \sum \iint_{S_i} \rho \vec{v} \cdot d\vec{S}_i = 0 \ , \tag{15}$$

$$\iiint_V \frac{\partial}{\partial t}(\rho \vec{v})\, dV + \sum \iint_{S_i} \rho \vec{v} \otimes \vec{v} \cdot d\vec{S}_i = - \sum \iint_{S_i} p\, d\vec{S}_i \ , \tag{16}$$

where the summation over surface integrals considers the cylinder shell and the two inflow and outflow planes with surface normal vectors $d\vec{S}_\perp = [r\ dr\ d\theta, 0, 0]^T$ and $d\vec{S}_\parallel = [0, R_c\ d\theta\ dx, 0]^T$ in cylindrical coordinates, respectively. Linearization upon a mean flow state with $p = p_0 + p'$, $\rho = \rho_0 + \rho'$, and $\vec{v} = \vec{v}_0 + \vec{v}' = [U_0, 0, 0]^T + [u', v', w']^T$ and using the isentropic expression $\rho' = p'/c_0^2$ allows to write the mass conservation Eq. (15) as:

$$\int_0^{2\pi} \int_0^{R_c} \int_{-\epsilon/2}^{+\epsilon/2} i\omega \frac{p'}{c_0^2} r\, dr\, dx\, d\theta \ + \ \left[\int_0^{2\pi} \int_0^{R_c} \left(\rho_0 U_0 + \rho_0 u' + U_0 \frac{p'}{c_0^2} \right) r\, dr\, d\theta \right]_L^R \ + \ \int_0^{2\pi} \int_{-\epsilon/2}^{+\epsilon/2} \rho_0 v' R_c\, dx\, d\theta \ = \ 0 \ , \tag{17}$$

where only first order terms are considered. The brackets represent subtraction of the borders $[a]_L^R \equiv a^R - a^L$ and the superscripts ^{R} and ^{L} denote values at axial positions $x = +\epsilon/2$ and $x = -\epsilon/2$, respectively. Due to axial symmetry, the integrals in the azimuthal direction can be canceled out. Furthermore, Since there is no discontinuity for the mean quantities over the connection plane, the first term in the brackets $\rho_0 U_0$ vanishes. In the presence of mean flow, the impedance boundary condition given by Myers [7]:

$$v' = \left(1 - i \frac{U_0}{\omega} \frac{\partial}{\partial x} \right) \left(\frac{p'}{Z} \right) \ , \tag{18}$$

has to be used to evaluate the surface integral on the cylinder shell:

$$\int_0^{2\pi} \int_0^{R_c} \int_{-\epsilon/2}^{+\epsilon/2} i\omega \frac{p'}{c_0^2} r\, dr\, dx\, d\theta + \left[\int_0^{2\pi} \int_0^{R_c} \left(\rho_0 u' + U_0 \frac{p'}{c_0^2} \right) r\, dr\, d\theta \right]_L^R + \int_0^{2\pi} \int_{-\epsilon/2}^{+\epsilon/2} \rho_0 R_c \frac{p'}{Z}\, dx - i \frac{\rho_0 U_0}{\omega} \int_0^{2\pi} \int_L^R d\left(\frac{p'}{Z} \right) d\theta = 0 \ . \tag{19}$$

The last term in the previous equation can readily be evaluated as $[-i\rho_0 U_0 \int p'/(\omega Z) d\theta]_L^R$. Following the compact approach of Gabard and Astley [12], the limit of Eq. (19) as $\epsilon \to 0$ is then considered. The first and third terms vanish and, as pointed out in [12], additional terms appear at interfaces with finite impedance $Z \neq \infty$. However, at this limiting case and due to the discontinuity caused by the different mode shapes across the jump, the conservation equations can only be weakly fulfilled. Following the Galerkin approach, the integral equations are weighted by a continuous function $\Psi(r, \theta)$:

$$\left[\int_0^{2\pi} \int_0^{R_c} \Psi \left(u' + M \frac{p'}{\rho_0 c_0} \right) r\, dr\, d\theta - \ i\, \Psi \frac{M c_0 R_c}{\omega} \int_0^{2\pi} \frac{p'}{Z}\, d\theta \right]_L^R \ = \ 0 \ , \tag{20}$$

where the axial Mach number $M = U_0/c_0$ is also used. Applying the same series of principles to the conservation of momentum yields after some rearrangement to:

$$\left[\int_0^{2\pi} \int_0^{R_c} \Psi \left(M u' \vec{e}_x + M \vec{v}' + (M^2 + 1) \frac{p'}{\rho_0 c_0} \vec{e}_x \right) r\, dr\, d\theta \ - \ i\Psi \frac{M^2 c_0 R_c}{\omega} \int_0^{2\pi} \frac{p'}{Z}\, d\theta\, \vec{e}_x \right]_L^R \ = \ 0 \quad . \tag{21}$$

Again, additional terms at interfaces with finite impedance arise. However, these can be replaced by substitution of the mass conservation Eq. (20) into Eq. (21). The three components of the weak form of the linearized momentum

equation can be finally written as:

$$\left[\int_0^{2\pi}\int_0^{R_c}\Psi\left(Mu' + \frac{p'}{\rho_0 c_0}\right) r\, dr\, d\theta\right]_L^R = 0 \quad ,$$
$$\left[\int_0^{2\pi}\int_0^{R_c}\Psi M v' r\, dr\, d\theta\right]_L^R = 0 \quad , \tag{22}$$
$$\left[\int_0^{2\pi}\int_0^{R_c}\Psi M w' r\, dr\, d\theta\right]_L^R = 0 \quad .$$

At this point, it is convenient to make a distinction between the case with and without mean flow. In the absence of mean flow, the conservation equations for the compact element simplify into:

$$\left[\int_0^{2\pi}\int_0^{R_c}\Psi u' r\, dr\, d\theta\right]_L^R = 0 \quad , \quad \left[\int_0^{2\pi}\int_0^{R_c}\Psi \frac{p'}{c_0\rho_0} r\, dr\, d\theta\right]_L^R = 0 \ , \tag{23}$$

with two relations for the sets of two unknowns. They correspond to the matching of pressure and axial velocity widely used in literature.

In the presence of axial mean flow the linearized momentum conservation equation delivers two additional relations for the characteristic amplitudes. We have four relations for two unknowns: one from Eq. (20) and three from Eq. (22). This means that for the general case with mean flow and taking care only of mass and momentum, the problem is overdetermined. To overcome this issue only the axial component of the momentum conservation Eq. (22) is considered. Up to first order, mass conservation inherits acoustic energy conservation, too. Concerning the acoustic intensity $I = u'p'$, which is second order in magnitude, additional relations are thus needed. The physical interpretation and the evaluation of the effects neglected by taking only the axial term is part of ongoing research.

Substitution of the general solution Eq. (2) in the chosen set of equations delivers the relations between the characteristic amplitudes on both sides of the jump. The temporal dependence $e^{-i\omega t}$ cancels out. Because of linearity and due to the axial symmetry, the tangential modes can be treated independently (the impedance is constant over the θ-coordinate). This means that no scattering into different tangential mode orders will occur. Furthermore, without loss of generality, the axial position $x = 0$ is used. In practice, only a finite number of N_r radial modes can be taken into account. The problem has thus $2 \times N_r$ unknowns, the $F_{mn}^{R/L}$ and $G_{mn}^{R/L}$ characteristic amplitudes on both sides of the discontinuity. The Galerkin approach using an orthogonal set of N_r weighting functions $\Psi_{m\nu}$ with $\nu = 0, 1, \ldots, N_r$ is used to close the problem. Note that the radial and axial wave numbers have different values on the left and on the right side of the connecting plane. To distinguish them, the soft-wall case will be denoted by a * superscript. The radial mode shapes of the hard-wall case build an orthogonal set and it is convenient to use them as weighting functions $\Psi_{m\nu} = J_m(\lambda_{m\nu} r)$. This leads to the following system of $2N_r$ equations:

$$\int_0^{R_c} J_m(\lambda_{m\nu} r) \sum_{n=0}^{N_r} \{J_m(\lambda_{mn} r)\left[(\kappa_{mn}^{+} M + 1) F_{mn} + (\kappa_{mn}^{-} M + 1) G_{mn}\right]\} r dr \quad =$$
$$\int_0^{R_c} J_m(\lambda_{m\nu} r) \sum_{n=0}^{N_r} \{J_m(\alpha_{mn}^{*+} r)(\kappa_{mn}^{*+} M + 1) F_{mn}^{*} + J_m(\alpha_{mn}^{*-} r)(\kappa_{mn}^{*-} M + 1) G_{mn}^{*}\} r dr$$
$$- i\, \frac{M c_0 R_c}{\omega} \frac{J_m(\lambda_{m\nu} R_c)}{Z} \sum_{n=0}^{N_r} \{J_m(\alpha_{mn}^{*+} R_c) F_{mn}^{*} + J_m(\alpha_{mn}^{*-} R_c) G_{mn}^{*}\} \quad , \tag{24}$$

$$\int_0^{R_c} J_m(\lambda_{m\nu} r) \sum_{n=0}^{N_r} \{J_m(\lambda_{mn} r)\left[(\kappa_{mn}^{+} + M) F_{mn} + (\kappa_{mn}^{-} + M) G_{mn}\right]\} r dr \quad =$$
$$\int_0^{R_c} J_m(\lambda_{m\nu} r) \sum_{n=0}^{N_r} \{J_m(\alpha_{mn}^{*+} r)(\kappa_{mn}^{*+} + M) F_{mn}^{*} + J_m(\alpha_{mn}^{*-} r)(\kappa_{mn}^{*-} + M) G_{mn}^{*}\} r dr \quad , \tag{25}$$

The integral terms can be evaluated analitically:

$$\zeta_{\nu n} = \int_0^{R_c} J_m(\lambda_{m\nu} r) J_m(\lambda_{mn} r) r \, dr = \begin{cases} \frac{R_c}{2}\left[1 - \left(\frac{m}{\lambda_{mn} R_c}\right)^2\right] J_m^2(\lambda_{mn} R_c) & \text{if } \nu = n; \\ 0 & \text{if } \nu \neq n. \end{cases} \tag{26}$$

$$\zeta_{\nu n}^{*\pm} = \int_0^{R_c} J_m(\lambda_{m\nu} r) J_m(\alpha_{mn}^{*\pm} r) r dr = \frac{R_c}{\lambda_{m\nu}^2 - \alpha^{*\pm 2}{}_{mn}} \left[\lambda_{m\nu} J_{m+1}(\lambda_{m\nu} R_c) J_m(\alpha_{mn}^{*\pm} R_c) - \alpha_{m\nu}^{*\pm} J_{m+1}(\alpha_{m\nu}^{*\pm} R_c) J_m(\lambda_{m\nu} R_c)\right] . \tag{27}$$

In matrix form notation and using the vectors $\vec{q} = [F_{m0}, G_{m0}, F_{m1}, G_{m1}, \ldots, F_{mN_r}, G_{mN_r}]^T$ on the hard-wall side and $\vec{q}^* = [F_{m0}^*, G_{m0}^*, F_{m1}^*, G_{m1}^*, \ldots, F_{mN_r}^*, G_{mN_r}^*]^T$ on the soft-wall side they can be written as:

$$\mathbf{Q}\vec{q} = \mathbf{Q}^* \vec{q}^* \quad , \tag{28}$$

with matrix entries:

$$Q(2\nu - 1, 2n - 1) = \zeta_{\nu n}(\kappa_{mn}^+ M + 1) \quad , \quad Q(2\nu - 1, 2n) = \zeta_{\nu n}(\kappa_{mn}^- M + 1) \quad , \tag{29}$$

$$Q(2\nu, 2n - 1) = \zeta_{\nu n}(\kappa_{mn}^+ + M) \quad , \quad Q(2\nu, 2n) = \zeta_{\nu n}(\kappa_{mn}^+ + M) \quad , \tag{30}$$

and:

$$Q^*(2\nu - 1, 2n - 1) = \zeta_{\nu n}^{*+}(\kappa_{mn}^{*+} M + 1) - i \frac{M c_0 R_c}{\omega Z} J_m(\lambda_{m\nu} R_c) J_m(\alpha_{mn}^{*+} R_c) , \tag{31}$$

$$Q^*(2\nu - 1, 2n) = \zeta_{\nu n}^{*-}(\kappa_{mn}^{*-} M + 1) - i \frac{M c_0 R_c}{\omega Z} J_m(\lambda_{m\nu} R_c) J_m(\alpha_{mn}^{*-} R_c) , \tag{32}$$

$$Q^*(2\nu, 2n - 1) = \zeta_{\nu n}^{*+}(\kappa_{mn}^{*+} M + 1) , \tag{33}$$

$$Q^*(2\nu, 2n) = \zeta_{\nu n}^{*-}(\kappa_{mn}^{*-} M + 1) . \tag{34}$$

Due to the orthogonality of the weighting functions, the matrix $\mathbf{Q}$ is diagonal. Using this notation, the transfer matrix of a jump in shell impedance can be finally expressed in terms of these two matrices. For the jump from the hard-wall into the soft-wall, the transfer matrix is $\mathbf{T}_{hs} = \mathbf{Q}^{-1}\mathbf{Q}^*$. For the jump in the opposite direction the transfer matrix is $\mathbf{T}_{sh} = (\mathbf{Q}^*)^{-1}\mathbf{Q}$.

4. Application

4.1 Test case configuration

For validation of the method proposed, a test case configuration shown in Fig. 5 is used. It consists of a soft-wall duct segment of length L and radius R with specific shell impedance z_{eq} and connected to two hard-wall segments of length l, each. The duct has a uniform flow of Mach number M and free field impedance $\rho_0 c_0$. The inlet and outlet boundaries are ideally set as non-reflecting. Furthermore, the system can be excited at position $x = 0$ with a forward traveling wave of arbitrary mode order f_{mn}. In the linear case, the system can easily be characterized by quasi one-dimensional

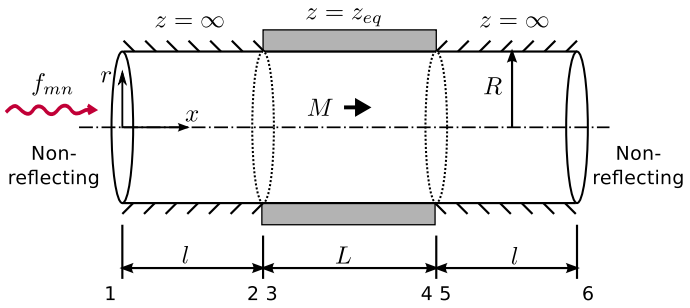

Figure 5: Test case configuration and characterization.

discrete elements, that link the characteristic amplitudes F_{mn} and G_{mn} at connecting planes. Since the geometry is axis-symmetric, each tangential mode order can be treated separately. Using the transfer matrix notation, each element

is mathematically described by a matrix $\mathbf{T}_{ab}$ that relates the amplitudes of the acoustic waves at positions a and b for given tangential mode order m:

$$\begin{pmatrix} f_{m0} \\ g_{m0} \\ \vdots \\ f_{mn} \\ g_{mn} \end{pmatrix}_b = \mathbf{T}_{ab} \begin{pmatrix} f_{m0} \\ g_{m0} \\ \vdots \\ f_{mn} \\ g_{mn} \end{pmatrix}_a \quad . \tag{35}$$

The advantage of this acausal notation, e.g. inputs and outputs of the system are not distinguished, is that the whole system can simply be built by multiplication of the individual transfer matrices:

$$\mathbf{T}_{16} = \mathbf{T}_{56}\, \mathbf{T}_{45}\, \mathbf{T}_{34}\, \mathbf{T}_{23}\, \mathbf{T}_{12} \quad , \tag{36}$$

where the indices 1 to 6 corresponds to the axial locations given in Fig. 5. For the three duct segments, the matrices are diagonal with exponential entries given by the corresponding axial wave numbers and segment lengths, respectively:

$$\mathbf{T}_{12} = \mathbf{T}_{56} = \begin{bmatrix} e^{-ik^{+}_{m0} l} & 0 & \cdots & 0 \\ 0 & e^{-ik^{-}_{m0} l} & & \vdots \\ \vdots & \ddots & \ddots & \\ & & e^{-ik^{+}_{mn} l} & 0 \\ 0 & \cdots & 0 & e^{-ik^{-}_{mn} l} \end{bmatrix} \quad , \quad \mathbf{T}_{34} = \begin{bmatrix} e^{-ik^{*+}_{m0} L} & 0 & \cdots & 0 \\ 0 & e^{-ik^{*-}_{m0} L} & & \vdots \\ \vdots & \ddots & \ddots & \\ & & e^{-ik^{*+}_{mn} L} & 0 \\ 0 & \cdots & 0 & e^{-ik^{*-}_{mn} L} \end{bmatrix} \quad . \tag{37}$$

For the jumps at the connecting planes, the matrices presented in Sec. 3.1 are used. In the general case, the previously mentioned matrices relate all radial orders in a tangential mode to each other. In practice, depending on how many radial modes are considered in the coupling, they are $2N_r \times 2N_r$ square matrices.

Physically, the scattering matrix notation offers a more descriptive characterization of the problem that preserves causality. In this case, the system is described by a matrix $\mathbf{S}_{ab}$ that relates the incoming to the outgoing waves at positions a and b:

$$\begin{pmatrix} f_{m0,b} \\ g_{m0,a} \\ \vdots \\ f_{mn,a} \\ g_{mn,b} \end{pmatrix}_{out} = \mathbf{S}_{ab} \begin{pmatrix} f_{m0,a} \\ g_{m0,b} \\ \vdots \\ f_{mn,a} \\ g_{mn,b} \end{pmatrix}_{in} = \begin{bmatrix} [2\times 2]_{0\to 0} & \cdots & [2\times 2]_{n\to 0} \\ [2\times 2]_{0\to 1} & & \vdots \\ \vdots & \ddots & \\ [2\times 2]_{0\to n} & & [2\times 2]_{n\to n} \end{bmatrix} \begin{pmatrix} f_{m0,a} \\ g_{m0,b} \\ \vdots \\ f_{mn,a} \\ g_{mn,b} \end{pmatrix}_{in} \quad . \tag{38}$$

The scattering matrix can be divided into $[2\times 2]$ sub-block matrices that allow a physical representation of the different entries. Each sub-block represents the coupling between two radial mode orders as shown by the arrows in the indices. Thus, for each sub-block, the diagonal entries represent transmission, while the off-diagonal elements reflection from and into the corresponding radial orders of the up- and downstream traveling waves. As an example consider the coupling of the radial order $n = 0$ into order $n = 1$:

$$[2\times 2]_{0\to 1} = \begin{bmatrix} T^{+}_{0\to 1} & R^{+}_{0\to 1} \\ R^{-}_{0\to 1} & T^{-}_{0\to 1} \end{bmatrix} \quad . \tag{39}$$

For the test case given in Fig. 5 with non-reflecting boundaries, the scattering matrix $\mathbf{S}_{16}$ gives the response of the system to the single mode excitation. The input vector has a single non zero entry $f_{mn_{ex}}$ for the chosen mode order. Knowing the response of the system at position 1, the amplitudes at the remaining locations 2 to 6 can be calculated using the individual transfer matrices. However, it is not trivial to derive the scattering matrix of a system from the individual element matrices. In this paper, a method based on matrix manipulation is used.

We start by expressing the state vector at position 6 in terms of incoming $\vec{x}_{in}$ and outgoing $\vec{x}_{out}$ vectors:

$$\begin{pmatrix} f_{m0} \\ g_{m0} \\ \\ \vdots \\ \\ f_{mn} \\ g_{mn} \end{pmatrix}_6 = \underbrace{\begin{bmatrix} 1 & 0 & & \cdots & & 0 & 0 \\ 0 & 0 & & & & & \\ & & 1 & & & & \\ \vdots & & & \ddots & & & \vdots \\ & & & & 0 & & \\ 0 & & & & & 1 & 0 \\ 0 & & & \cdots & & 0 & 0 \end{bmatrix}}_{\mathbf{E}^1} \underbrace{\begin{pmatrix} f_{m0,6} \\ g_{m0,1} \\ \\ \vdots \\ \\ f_{mn,6} \\ g_{mn,1} \end{pmatrix}}_{\vec{x}_{out}} + \underbrace{\begin{bmatrix} 0 & 0 & & \cdots & & 0 & 0 \\ 0 & 1 & & & & & \\ & & 0 & & & & \\ \vdots & & & \ddots & & & \vdots \\ & & & & 1 & & \\ 0 & & & & & 0 & 0 \\ 0 & & & \cdots & & 0 & 1 \end{bmatrix}}_{\mathbf{E}^2} \underbrace{\begin{pmatrix} f_{m0,1} \\ g_{m0,6} \\ \\ \vdots \\ \\ f_{mn,1} \\ g_{mn,6} \end{pmatrix}}_{\vec{x}_{in}} \quad . \tag{40}$$

Table 1: Geometrical and thermodynamical parameters of the test case.

$R\ [m]$	$L\ [m]$	$l\ [m]$	$c_0\ [m/s]$	$\rho_0\ [kg/m^3]$	$f_{bpf}\ [Hz]$	$h\ [m]$	$m_b\ [-]$
1	0.8	0.15	340	1.2	1680	0.035	24

Doing the same for the state vector at position 1, we can write the transfer matrix notation as:

$$\mathbf{E}^1 \vec{x}_{out} + \mathbf{E}^2 \vec{x}_{in} = \mathbf{T}_{16}(\mathbf{E}^1 \vec{x}_{in} + \mathbf{E}^2 \vec{x}_{out}) \quad . \tag{41}$$

After some rearrangement, the scattering matrix notation is given by:

$$\vec{x}_{out} = (\mathbf{E}^1 - \mathbf{T}_{16}\, \mathbf{E}^2)^{-1}\, (\mathbf{T}_{16}\, \mathbf{E}^1 - \mathbf{E}^2)\vec{x}_{in} \quad . \tag{42}$$

This method can be applied for any transfer matrix. However, the inversion of the matrix given by expression $(\mathbf{E}^1 - \mathbf{T}_{16}\, \mathbf{E}^2)^{-1}$ can be mathematically difficult if the transfer matrix is ill-conditioned. This can happen for systems in which some radial orders are highly evanescent. Thus, the number of radial mode orders considered for the analysis is restricted by the accuracy of the method used for matrix inversion.

4.2 Validation: noise suppression in aeroengines

To validate the mode matching method proposed in this paper, a test case configuration given by McAlpine et al. [8] is used. Table 1 list the geometrical and physical properties of the configuration. It corresponds to the inlet of a turbofan engine equipped with partial lining for noise suppression. McAlpine et al. assumed that the system is excited by the rotor-alone mode of tangential order $m = m_b$ and $n = 0$ at a frequency equal to the blade passing frequency f_{bpf}:

$$f^{ex}_{m_b 0} = |A_{ex}| J_m(\lambda_{m_b 0} r/R) e^{i m_b \theta} e^{-i 2\pi f_{bpf} t} \quad . \tag{43}$$

The specific acoustic impedance of the lining (soft-wall duct segment) is given as:

$$z_{lin} = 3 - i \cot(h\omega/c_0) \quad . \tag{44}$$

In their study, they simulated the acoustic field excited at the blade passing frequency using the finite element code ACTRAN/AE[1].

We solved the same system using the mode matching method and solution procedure proposed in this paper and compare them against the FEM analysis of McAlpine et al. Figure 6 and 7 show the radial distribution of the normalized acoustic pressure at the axial positions of the two jumps in shell impedance, respectively. The distribution given by the FEM analysis is compared against the two distributions just up- and downstream of the jumps given by the mode matching technique considering $N_r = 6$ radial modes in the coupling. On most of the regions good agreement can be seen. Only close to the boundary at position $r \approx R$ some discrepancies arise. However, this is in accordance to the mode matching technique, which allows local discontinuities across jumps in order to satisfy the radial boundary condition. On the hard-wall side it can be seen that the radial gradient is zero leading to zero radial velocity. In contrast, on the soft-wall side the gradient is not zero.

Figure 8 shows the normalized wall pressure distribution along the axial direction. The agreement with the FEM data is also good in most of the regions. The biggest discrepancies are located close to the first jump. However, as already seen in the radial distributions, these discrepancies concentrate in the vicinity of the shell boundary.

4.3 Representative resonator ring

We now continue with the application of the mode matching technique to a resonator ring modeled as soft-wall section with homogeneous equivalent shell impedance given by Eq. (14) and Eq. (12). The test case characterized in Fig. 5 is used again but choosing parameters representative of modern rocket thrust chambers. Table 2 gives the non-dimensionalized parameters for both the equivalent impedance and test case configuration.

The requirements on resonator rings for stabilization of rocket thrust chambers are considerable different compared to those on linings in turbofan engines. Firstly, the relevant tangential mode orders are much lower. Most chambers are prone to instabilities of the mode orders $m = 0$ and $m = 1$. Secondly, the resonant frequency of the coupled system is in general not known a priori. It may even change during operation. Thus, resonator rings should work not only for one definite frequency, but rather within a frequency range.

[1] Free Field Technologies S.A., http://www.fft.be

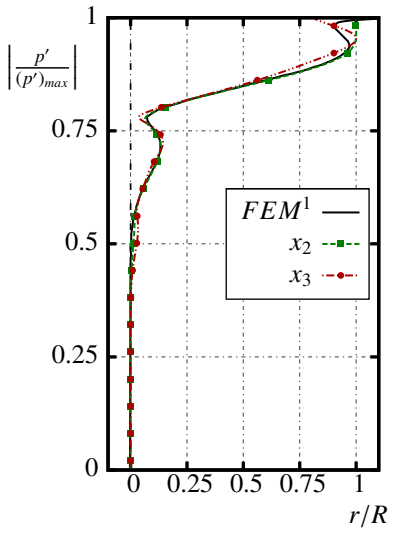

Figure 6: Normalized acoustic pressure at axial position $x = l$. Full line: FEM distribution from [8]. Dashed lines: x_2 just upstream and x_3 just downstream of the first jump. Number of radial modes considered, $N_r = 6$.

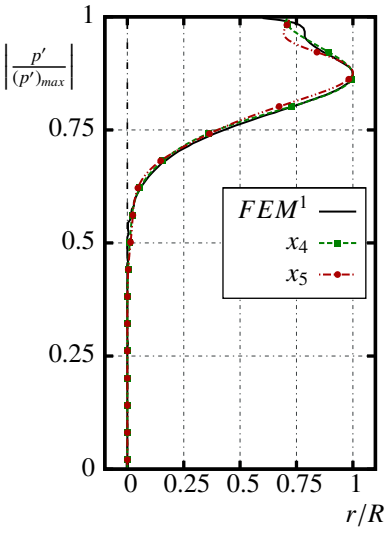

Figure 7: Normalized acoustic pressure at axial position $x = l + L$. Full line: FEM distribution from [8]. Dashed lines: x_4 just upstream and x_5 just downstream of the first jump. Number of radial modes considered, $N_r = 6$

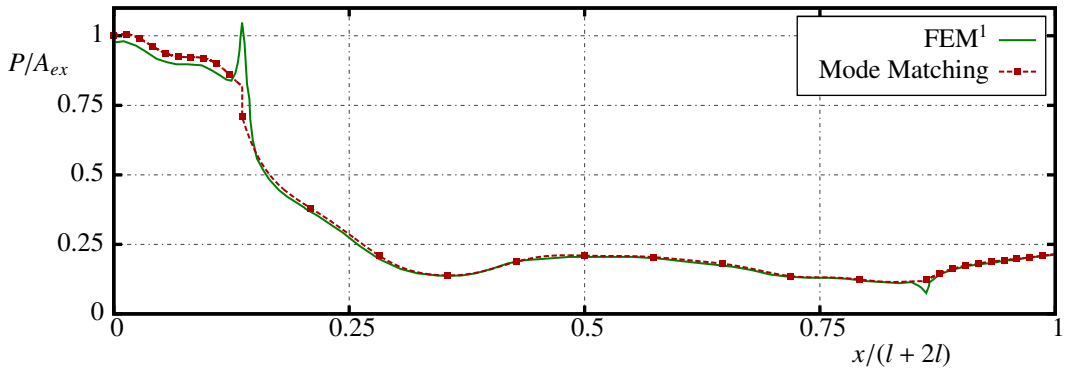

Figure 8: Normalized acoustic pressure at the wall for $r = R$. Full line: FEM distribution from [8]. Dashed line: mode matching considering $N_r = 6$ radial modes for the coupling.

The frequency dependent scattering matrix describes the response of the resonator to traveling waves in the frequency range of interest. As already mentioned in Sec. 4.1, the scattering matrix of a soft-wall duct segment can be divided into $[2 \times 2]$ sub-blocks that describe the mode coupling in terms of transmission and reflection coefficients. However, radial modes are in most of the cases cut-off and are thus present only close to impedance discontinuities. The first column of sub-block matrices describe the coupling of the f_{m0} and g_{m0} waves into higher radial orders $f_{m0\ldots N_r}$ and $g_{m0\ldots N_r}$.

Figure 9 shows the transmission and reflection coefficients of the scattering matrix for the tangential mode order $m = 0$. Only the first three $[2 \times 2]_{0\to n}$ sub-blocks of the first column are shown, $n = 0$ to $n = 2$. They correspond to the coupling of the plane wave to higher radial modes. The frequency is non-dimensionalized by the resonant frequency of the cavities $f_R = \bar{c}/(4l_e)$. As expected, close to the eigenfrequency of the cavities, the resonator ring reduces the transmission coefficients and at the same time increases the reflection. Furthermore, scattering into higher radial mode

Table 2: Parameters used in the resonator ring test case. For generality, quantities are given in non-dimensional form.

ϵ_{nl}	l_r/R_c	l_e/R_c	d/R_c	$\bar{c}/c$	n_R	M	L/R	l/R
40	0.205	0.571	0.089	0.654	22	0.25	0.089	0.022

orders is also clearly observed. This is because at this frequency the mode shapes in the soft-wall segment differ more strongly from those of in the hard-wall section. As expected, the contribution of the diagonal elements is biggest.

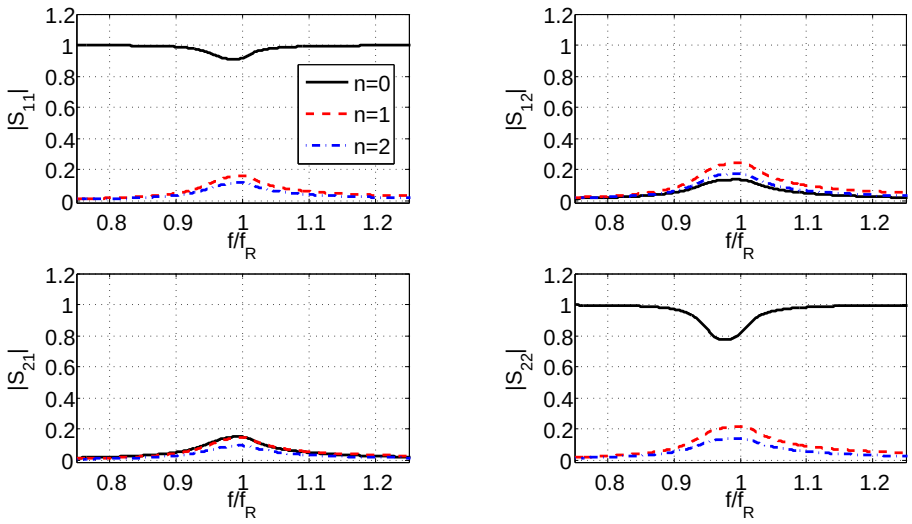

Figure 9: First column of sub-blocks from scattering matrix, tangential mode order $m = 0$.

As seen in Fig. 10 the behavior is considerably different for the first tangential order $m = 1$. For this mode the cut-on frequency corresponds approximately to the eigenfrequency of the cavities $f^c_{10}/f_R \approx 1$. Again, the first three sub-blocks of the scattering matrix are shown. Coupling to higher radial modes is also seen in this tangential order, however not as strong as in the plane wave case. The transmission of the acoustic waves with radial order $n = 0$ has a peak at frequencies slightly lower than the eigenfrequency of the cavities. At these frequencies the tangential mode is still cut-off. Nevertheless, the peak reaches values larger than unity, suggesting that the propagation of the wave is actually enhanced by the resonator ring. The reflection coefficients are also high in this frequency range. At yet higher frequencies the resonator rings start to reduce the amplitudes of the traveling waves. However, it is not totally clear at the time of writing this paper how the additional pressure level is generated. A remaining question is whether this behavior is actually physical or is rather a sort of singularity of the mode matching technique. The assessment of this issues is part of the ongoing research.

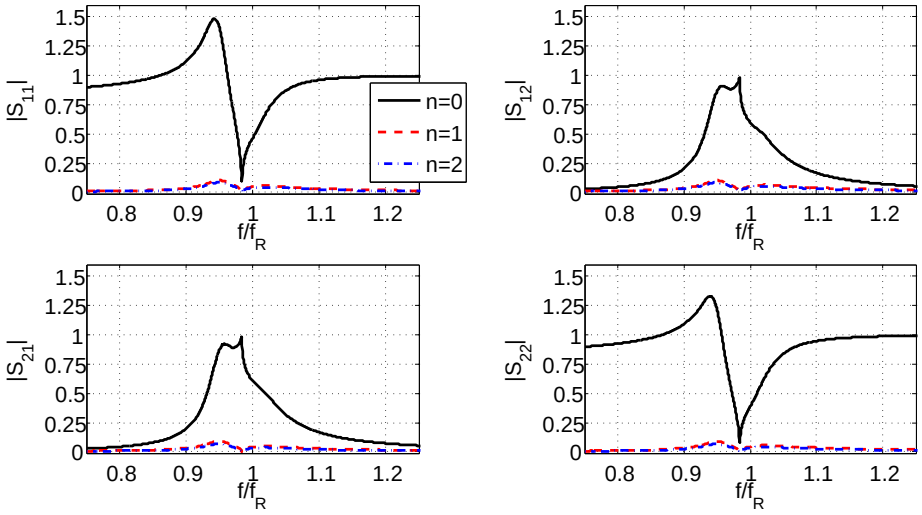

Figure 10: Tangential mode order $m = 1$.

5. Conclusions and future work

A previously proposed resonator ring element composed of cylindrical duct segments with reactive and dissipative shell boundary, has been extended to account for scattering and mode coupling of three dimensional acoustic waves at duct junctions. Taking mean flow into account, the conservation of mass and momentum is weakly fulfilled up to first order in an integral sense using the Galerkin approach. For a generic test case of a turbofan inlet equipped with partial lining, the method is validated against FEM data available from the literature. For the test case considered, the agreement is very good and the mode matching method is able to reproduce the pressure distribution.

The scattering matrix of a representative resonator ring as used in modern rocket thrust chambers is subsequently studied. A wave reaching the resonator is partially transmitted and partially reflected at the interfaces between duct segments of different shell impedance. Furthermore, a mode coupling mechanism appears, which transfers acoustic energy into higher mode orders, especially if the acoustic mode shapes in the resonator ring differ strongly from their hard-wall duct counterparts. The consequences of this mode coupling are not necessarily straightforward and depend actually on the tangential mode order considered.

For the tangential order $m = 0$, close to the eigenfrequency of the cavities f_R, the propagation of plane waves is clearly diminished. This can be attributed to the resistance or real part of the impedance expression used as shell boundary condition, which inherits the viscous and turbulent dissipation losses caused by the cavities. These losses can directly contribute to the stabilization of the thrust chamber. At the same time, reflection into higher radial mode orders occur.

In contrast, for the tangential order $m = 1$, two regions arise with opposite response. At frequencies below cut-on, the propagation of the acoustic waves is enhanced by the influence of the resonator. Reflection into radial modes of higher order also occurs, however, not as strong as in the plane wave case. It is not until frequencies beyond cut-on where the propagation of waves is reduced. The physical interpretation of this ambivalent behavior is not totally clarified yet. While some instabilities at the interface might be responsible for this behavior, it still has to be verified whether this effect is not caused by a singularity in the mode matching technique. The answer to these questions is part of the ongoing research.

The extended resonator ring element can be applied in a complete stability analysis of the thrust chamber taking the major driving and damping mechanisms into account and using the network element method as proposed in [2].

Acknowledgments

Financial support has been provided by the German Research Foundation (Deutsche Forschungsgemeinschaft – DFG) in the framework of the Sonderforschungsbereich Transregio 40, project A3.

References

[1] Cárdenas Miranda, A. and Polifke, W. 2010. Effects of temperature inhomogeneity on the damping characteristics of quarter wave resonator rings. *SFB-TRR40 Annual Report 2010*, 41–54.

[2] Cárdenas Miranda, A. and Polifke, W. 2011. Damping characteristics of resonator rings with application to low order stability prediction of rocket thrust chambers. In: *Proceedings of the 4th European Conference for Aerospace Sciences (EUCASS)*, St. Petersburg, Russia.

[3] Gabard, G. 2010. Mode-Matching techniques for sound propagation in lined ducts with flow. In: *Proceedings of the 16th AIAA/CEAS Aeroacoustic Conference*.

[4] Law, T.R., Dowling, A.P. and Corral, R. 2010. Optimisation of axially segmented liners for aeroengine broadband noise. *J. Sound and Vibration*, **329**, 4367–4379.

[5] Rienstra, S.W. 2002. A classification of duct modes based on surface waves. *Wave Motion*, **37**, 119–135.

[6] Rienstra, S.W. 2007. Acoustic scattering at a hard-soft lining transition in a flow duct. *J. Engineering Math*, **59**, 451–475.

[7] Myers, M.K. 1980. On the acoustic boundary condition in the presence of flow. *J. Sound and Vibration*, **71**, (3), 429–434.

[8] McAlpine, A., Astley, R.J., Hii, V.J.T., Baker, N.J. and Kempton, A.J. 2006. Acoustic scattering by an axially-segmented turbofan inlet duct liner at supersonic fan speeds. *J. Sound and Vibration*, **294**, 780–806.

[9] Laudien, E., Pongratz, R., Pierro, R. and Preclik, D. 1995. Experimental procedures aiding the design of acoustic cavities. *Liquid Rocket Engine Combustion Instability*, **169**, 377–399.

[10] Marino, P.A., Bohn, N.,Russell, P.L., Schnell, A.C and Parsons, G.L. 1967. A study of the suppression of combustion oscillations with mechanical damping devices. *NASA Technical Report CR-90094*.

[11] Munjal, M.L. 1987. Acoustics of ducts and mufflers. *John Wiley & Sons*.

[12] Gabard, G., Astley, R.J. 2008. A computational mode-matching approach for sound propagation in three-dimensional ducts with flow. *J. Sound and Vibration*, **315**, 1103–1124.